

High-Speed Single-Particle Tracking of GM1 in Model Membranes Reveals Anomalous Diffusion due to Interleaflet Coupling and Molecular Pinning

Katelyn M. Spillane,^{†,||} Jaime Ortega-Arroyo,^{†,||} Gabrielle de Wit,[†] Christian Eggeling,[‡] Helge Ewers,[§] Mark I. Wallace,[†] and Philipp Kukura^{†,*}

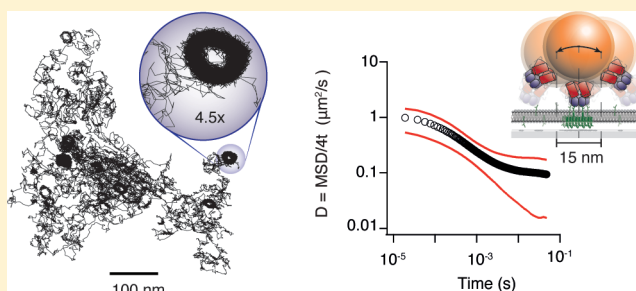
[†]Physical and Theoretical Chemistry Laboratory, Department of Chemistry, University of Oxford, South Parks Road, Oxford OX1 3QZ, United Kingdom

[‡]MRC Human Immunology Unit and Wolfson Imaging Centre Oxford, Weatherall Institute of Molecular Medicine, University of Oxford, Oxford OX3 9DS, United Kingdom

[§]Randall Division of Cell and Molecular Biophysics, King's College, London SE1 1UL, United Kingdom

ABSTRACT: The biological functions of the cell membrane are influenced by the mobility of its constituents, which are thought to be strongly affected by nanoscale structure and organization. Interactions with the actin cytoskeleton have been proposed as a potential mechanism with the control of mobility imparted through transmembrane “pickets” or GPI-anchored lipid nanodomains. This hypothesis is based on observations of molecular mobility using various methods, although many of these lack the spatiotemporal resolution required to fully capture all the details of the interaction dynamics. In addition, the validity of certain experimental approaches, particularly single-particle tracking, has been questioned due to a number of potential experimental artifacts. Here, we use interferometric scattering microscopy to track molecules labeled with 20–40 nm scattering gold beads with simultaneous <2 nm spatial and 20 μ s temporal precision to investigate the existence and mechanistic origin of anomalous diffusion in bilayer membranes. We use supported lipid bilayers as a model system and demonstrate that the label does not influence time-dependent diffusion in the small particle limit (≤ 40 nm). By tracking the motion of the ganglioside lipid GM1 bound to the cholera toxin B subunit for different substrates and lipid tail properties, we show that molecular pinning and interleaflet coupling between lipid tail domains on a nanoscopic scale suffice to induce transient immobilization and thereby anomalous subdiffusion on the millisecond time scale.

KEYWORDS: Anomalous diffusion, interferometric scattering microscopy, single-particle tracking, interleaflet coupling



The plasma membrane of all cells comprises two leaflets of distinct molecular composition and function. Even small changes in the lateral organization of its components can lead to dramatic effects on cellular function, including immune synapse formation,¹ bacterial chemotaxis,² and receptor clustering induced by pathogens with tightly spaced polyvalent binding sites.³ It remains largely unclear, however, how events such as a receptor binding to an extracellular leaflet lipid, or the spatial rearrangement of membrane components in the absence of transmembrane proteins,⁴ are communicated across a bilayer. Several mechanisms have been proposed⁵ based on line tension,^{6–9} direct interaction of lipids across the bilayer,^{10,11} molecular pinning,¹² and the transient formation of cholesterol-containing, ordered membrane domains,¹³ possibly caused by a picket-fence structure of the plasma membrane. Although these mechanisms differ in their nature, all are thought to result in anomalous diffusion of membrane proteins and lipids in the presence of immobile obstacles, transient binding or spatially nonuniform mobilities.

Because the lateral mobility of lipids in membranes is extremely fast, a series of advanced imaging techniques have been applied to investigate the existence, origin, and role of anomalous diffusion in bilayer membranes. Super-resolved fluorescence correlation spectroscopy has revealed anomalous diffusion of lipids in live cell membranes on the nanoscopic scale.¹⁴ High-speed single-particle tracking (SPT) of 40 nm diameter gold nanoparticle (AuNP) labels at 40 kHz frame rates and a localization precision of few tens of nanometers consistently revealed anomalous diffusion on the ~ 0.1 –10 ms time scale in living cells.¹⁵ Measurements of different cell types and membrane components led to a model based on compartments of varying sizes that restrict diffusion and result in a time-dependent diffusion coefficient.¹⁶ SPT with scattering labels, however, has been suggested to be susceptible to a series

Received: July 6, 2014

Revised: August 8, 2014

Published: August 18, 2014

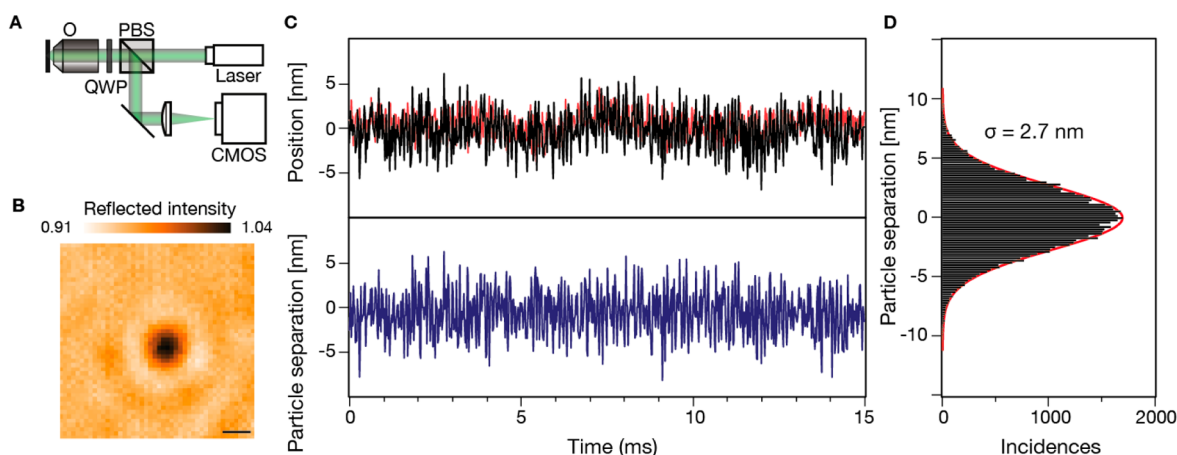


Figure 1. High-speed nanometric tracking of gold nanoparticles with iSCAT. (A) Schematic of the experimental setup. PBS, polarizing beamsplitter; QWP, quarter waveplate; O, oil-immersion microscope objective with a numerical aperture of 1.42. (B) Representative interferometric scattering image of a single 20 nm gold nanoparticle after subtraction of a median background.²² Scale bar: 500 nm. (C) Time traces of the positions of two immobilized 20 nm gold nanoparticles acquired with 10 μ s exposure time at 50 kHz frame rate (black and red, upper panel). Subtracting these two traces removes the nanometer motion due to vibrations and drift to yield the true localization error of the measurement (blue, lower panel). (D) Histogram of the interparticle distance from the time traces in C ($N = 5 \times 10^4$). The single-particle localization precision equates to $\sigma/2^{1/2} = 1.9$ nm, where σ is the full width at half-maximum.

of potential artifacts due to label size¹⁷ and poor localization precision.¹⁸ In addition, SPT with a molecular-sized fluorescent dye as a label did not reveal any signs of anomalous behavior down to the 300 μ s time scale, suggesting that the particle may be responsible for non-Brownian behavior.¹⁹ Finally, local nanoscopic membrane roughness has recently been put forward as an alternative explanation for the observation of anomalous diffusion in cells.²⁰

To clarify the source of these inconsistent and contradictory results, we designed a SPT assay with superior spatiotemporal resolution and precise control over the membrane roughness, its constituents and their interaction with the environment. Such an assay would allow one to investigate the mechanistic origin of anomalous diffusion, as well as any effects caused by the label. Our assay uses interferometric scattering microscopy (iSCAT)^{21,22} to track molecules labeled with 20–40 nm scattering gold beads with simultaneous <2 nm spatial and 20 μ s temporal precision. Given the complexity of cellular membranes, we chose supported lipid bilayers (SLBs) composed of 1,2-dioleoyl-*sn*-glycero-3-phosphocholine (DOPC) as a well understood and reproducible model membrane²³ and tracked the motion of the ganglioside GM1 doped at low concentration (0.03 to 1 mol %) on different substrates. Although SLBs represent highly simplified versions of cellular membranes, they have been used extensively in bottom-up studies of the structure and dynamics of bilayer membranes to elicit direct causation of observed behavior.²³ We chose GM1 due to its involvement in a wide range of cellular processes mediated by the plasma membrane such as endocytosis,^{24,25} B cell signaling,²⁶ and membrane domain formation.²⁷ The observation of cholera toxin-induced clustering of GM1 and ensuing phase segregation,²⁸ the role of GM1 as an established marker for liquid-ordered domains,²⁹ and the observation that GM1 diffuses anomalously in the plasma membrane of living cells due to transient molecular interactions,^{13,30} make it an archetypal system for studying lipid clustering and lateral lipid–lipid interactions.

Using iSCAT^{21,22} we followed the motion of GM1 in SLBs using AuNPs functionalized with cholera toxin B subunits

(CTxB), which can bind up to five GM1 molecules. A recent study on a similar model system using iSCAT revealed anomalous diffusion, including transient 20 nm confinements, although the temporal resolution (1 ms) was insufficient to deduce the underlying cause.³¹ In the current work, we have achieved a 50-fold increase in temporal resolution (20 μ s) with simultaneous <2 nm spatial precision, allowing us to observe lipid mobility with high spatiotemporal detail. We found that a combination of proximal GM1 interaction with a plasma-treated substrate and GM1 hydrocarbon chain saturation were sufficient to induce transient immobilization and subdiffusion on the sub-millisecond time scale. Spatiotemporal analysis of the confinement events suggests that confinement occurs on the <10 nm scale, consistent with temporary immobilization (molecular pinning) of GM1-bound CTxB. We conclude that instead of lateral lipid–lipid interactions in the plane of the membrane, interleaflet lipid–lipid interactions could control the clustering and motion of GM1 molecules in lipid bilayers.

Results. To achieve the imaging speed and localization precision required to fully characterize the transient mobilities of membrane constituents, we optimized interferometric scattering microscopy^{21,32} for high-speed imaging. The apparatus used here for high-speed iSCAT imaging is remarkably simple: a linearly polarized illumination beam passes through a polarizing beamsplitter and a quarter waveplate before entering a microscope objective. Light scattered by the sample interferes with the weak reflection at the membrane–water interface, and this light is collected by the same objective before being imaged onto a CMOS camera (Figure 1A). In previous applications of iSCAT, imaging speeds of up to 1 kHz were achieved by scanning the incident light over a large sample area (tens of μm^2) using acousto-optic deflectors. Here, by simply underfilling the objective to create a field of view of a few μm^2 , we are able to record trajectories containing tens of thousands of data points with a 50-fold increase in temporal resolution. In this experimental arrangement, 20 nm AuNPs appear as a clear drop of $\sim 9\%$ in the reflected beam intensity relative to that of the incident light (Figure 1B).

In contrast to fluorescence imaging, where the localization precision scales with the number of photons detected from the emitter,³³ the precision of iSCAT is governed by the ratio of the shot-noise-induced fluctuations in the background light intensity to the size of the iSCAT signal²² and can be tuned by adjusting the incident power and magnification of the imaging system. To avoid difficulties arising from nonstandard point spread functions common to interferometric imaging techniques with coherent light sources,³⁴ we determined the localization precision by recording the relative motion of two 20 nm particles immobilized on a cover glass (Figure 1C). Assuming that the particles are completely immobile, the fluctuations in the interparticle distance return a single-particle localization precision of 1.9 nm at an exposure time of only 10 μ s with heating of the particle surface of less than 1.5 K at the incident power density used.²² While state-of-the-art fluorescence microscopy can also achieve 1 nm precision, this comes at the expense of acquisition speed due to the limited achievable photon flux. Likewise, dark-field microscopy has been used to track light scattered from gold nanoparticle labels at 40 kHz frame rate (25 μ s exposure time), although with a localization precision of only 17 nm.¹⁵ Thus, iSCAT achieves an unprecedented combination of localization precision and speed with nanoscopic probes.

We first examined the diffusion of 20 nm AuNP/CTxB bound to GM1 in a SLB made from DOPC doped with 0.03 mol % GM1 on a plasma-cleaned glass substrate. CTxB is coupled to AuNPs through a biotin–streptavidin linker, and we estimate that a 20 nm AuNP has approximately 25 bound CTxB. Although a 20 nm AuNP is much larger (\sim 50 MDa) than the single-molecule fluorescent probes more typically used in tracking measurements, such as GFP (27 kDa), its size does not significantly affect receptor diffusion as the viscous forces of the membrane dominate the movement of the AuNP/CTxB complex. Smaller nanoparticle labels on the order of 10 nm or below could also be imaged and tracked,²² although in this case we used larger particles to ensure confident differentiation from residual vesicles that are sometimes encountered on the bilayer surface.

Tracking the AuNP at 50 kHz with 10 μ s exposure time, we acquired trajectories that reveal circular nanoscopic regions of confinement, suggesting anomalous behavior (Figure 2A). To examine the time dependence of particle mobility quantitatively, we calculated the mean-square displacement (MSD) as a function of the time interval.³⁵ Using the relationship $\text{MSD} \propto \Delta t^\alpha$, we can classify the motion of the particle based on the value of the anomalous diffusion coefficient α , with $\alpha = 1$ indicating Brownian diffusion and $\alpha \neq 1$ suggesting anomalous diffusion. A logarithmic plot of the diffusion coefficient versus time has the slope $(\alpha - 1)$ and thus provides a convenient representation of the nature of the motion: a slope of zero indicates Brownian diffusion, while negative and positive slopes represent sub- and superdiffusion, respectively. According to this analysis, CTxB bound to GM1 in a SLB formed on plasma-cleaned glass exhibits subdiffusive lateral motion on the 20 μ s to 10 ms time scale and Brownian diffusion at longer times (Figure 2A). In contrast to previous reports where such data showing the transition from anomalous to Brownian diffusion had to be generated from separate measurements at different acquisition speeds,¹⁶ these plots were constructed from single events using a maximum time lag equal to 20% of the trajectory length, thus spanning almost 5 orders of magnitude in time. The circle markers show the mean time-dependent diffusion

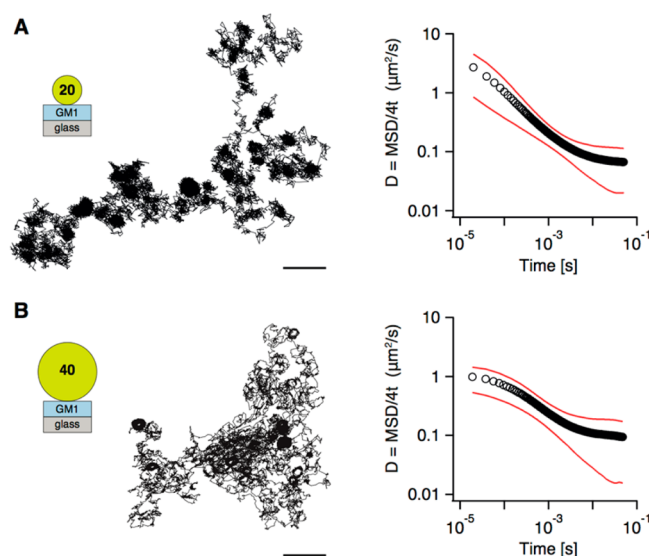


Figure 2. Anomalous subdiffusion of GM1 in supported lipid bilayers on glass substrates. Sample trajectories and time-dependent mobilities of (A) 20 nm AuNP/CTxB/GM1 on glass and (B) 40 nm AuNP/CTxB/GM1 on glass. The open circles represent the mean behavior of all acquired trajectories, and the red lines the standard deviation resulting from inhomogeneous broadening. Scale bars: 100 nm. Total number of frames used for the log–log plots: (A) 1.75×10^6 and (B) 2.05×10^6 . Number of data points per trajectory: 5×10^4 .

coefficient of 35 trajectories, while the red lines indicate the range of observed behaviors (one standard deviation). This diffusion analysis demonstrates that CTxB-bound GM1 diffusion is confined on short (<10 ms) time scales. The macroscopic diffusion coefficient ($0.09 \mu\text{m}^2/\text{s}$) for time lags longer than 10 ms agrees well with independently recorded results for fluorescently labeled CTxB on an identical SLB with fluorescence correlation spectroscopy ($0.14 \pm 0.01 \mu\text{m}^2/\text{s}$).³⁰ iSCAT experiments with 40 nm particles resulted in similar trajectories and time-dependent mobilities with minor differences for sub-ms time lags (Figure 2B).

In the experiments described above, the membrane supports were cover glass subjected to oxygen plasma cleaning, a process known to functionalize the surface with hydroxyl groups that are capable of immobilizing the hydroxyl-containing GM1 head groups in the lower leaflet.^{30,36} To investigate the potential origin of the observed anomalous behavior, we modified the membrane–substrate interaction and the degree of potential interleaflet coupling while keeping modifications to the assay to a minimum. First, we repeated our GM1 tracking experiments using chemically inert mica as a substrate. Because of difficulties with removing all membrane-proximal vesicles on mica, and because lipid vesicles and 20 nm AuNPs have similar signal contrasts in iSCAT, we used 40 nm labels to ensure that all tracked objects corresponded to CTxB/GM1. During the acquisition of more than 5×10^5 frames we observed no confinement events and exclusively Brownian motion for time delays $>100 \mu$ s (Figure 3A). For delays $<100 \mu$ s, we observed superdiffusive behavior, which we attribute to dynamic error in our measurements at early times due to the sub-nanometer localization precision achieved for 40 nm particles.³⁷ When superimposed on a subdiffusive slope, this effect results in a leveling off that resembles Brownian diffusion (Figure 2B). For 20 nm particles, where the localization precision was lower (2 nm), this effect was not observed (Figure 2A). To investigate

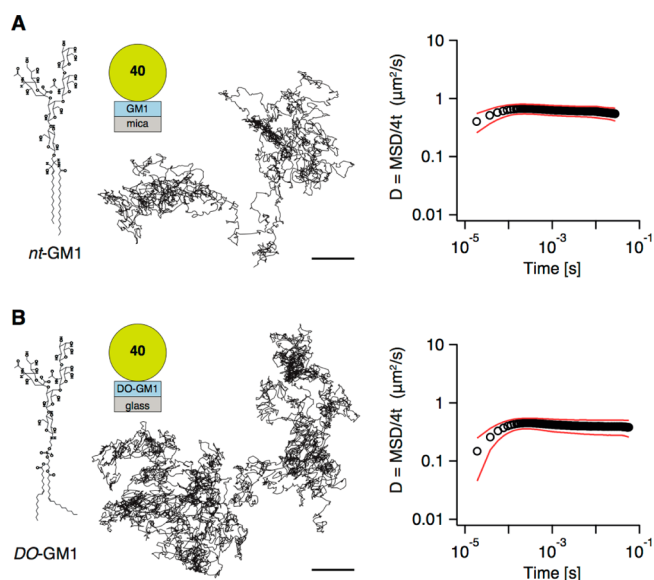


Figure 3. Brownian motion of GM1 in supported lipid bilayers on mica substrates and with modified lipid tail groups. Sample trajectories and time-dependent mobilities of (A) 40 nm AuNP/CTxB/nt-GM1 on mica and (B) 40 nm AuNP/CTxB/DO-GM1 on glass. The change in lipid tail structure upon modification of nt-GM1 is indicated by the molecular structures. Number of data points per trajectory: 2×10^4 . Scale bars: 100 nm. Total number of data points used for constructing log–log plots: (A) 3.1×10^5 , (B) 1.07×10^6 .

the reason for anomalous diffusion further, we modified the degree of interleaflet coupling between GM1 hydrocarbon chains by replacing the native GM1 (nt-GM1) with an analogue (DO-GM1) that has the unsaturated glycerophospholipid 1,2-dioleoyl-*sn*-glycero-3-phosphoethanolamine (DOPE) in place of the naturally occurring sphingosine base. Tracking the motion of DO-GM1 on plasma-cleaned glass substrates using 40 nm AuNPs revealed purely Brownian diffusion at delays $>100 \mu\text{s}$ as well. Upon examination of individual trajectories for DO-GM1 on glass, we found only extremely rare and short-lived binding events that under a macroscopic diffusion analysis were representative of Brownian motion (Figure 3B). This switch from anomalous to Brownian diffusion was observed although the interaction between the headgroup and the plasma-cleaned glass substrate remained unchanged from the nt-GM1 measurements. The comparison of nt-GM1 and DO-GM1 on plasma-cleaned glass demonstrates that surface roughness is unlikely to be the cause of anomalous diffusion, which is further supported by AFM measurements of the plasma-treated glass surface that show the RMS roughness to be only 0.6 nm.

We next examined the dependence of confinement on GM1 concentration by determining the fraction of time the particle was confined relative to the total length of each trajectory. For nt-GM1 on plasma-treated glass, the mean confined fraction for all GM1 concentrations measured (0.03–1 mol %) was 0.72 ± 0.03 with zero representing no confinement and one completely immobilized (Figure 4A). CTxB was considered to be confined when the label traveled less than 50 nm in 10

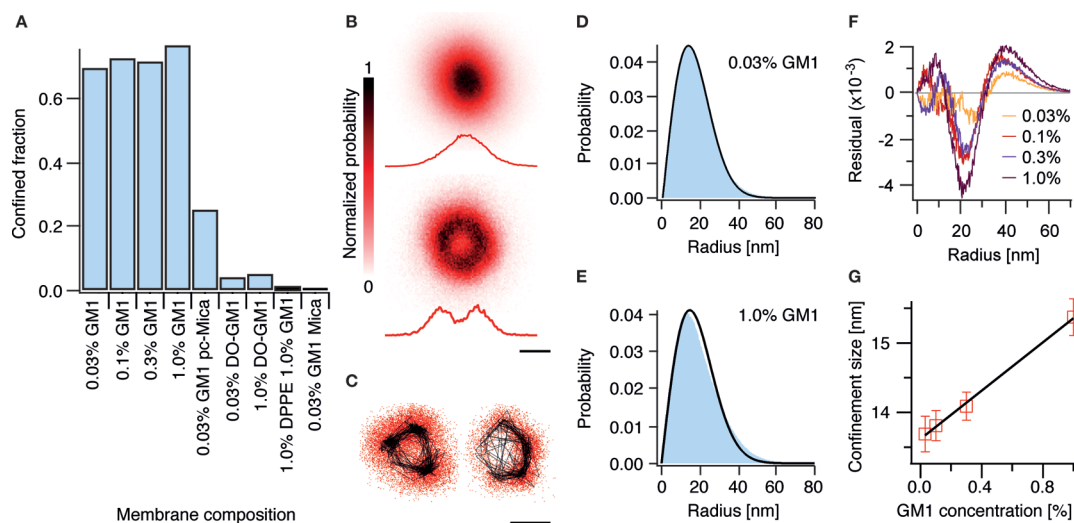


Figure 4. Analysis of transient immobilization events. (A) Confined fraction for different nt-GM1 concentrations in DOPC SLBs on glass, synthetically modified GM1 (DO-GM1) on glass, DPPE with a biotin/streptavidin linker in the presence of nt-GM1 on glass, and nt-GM1 on freshly cleaved and plasma-cleaned mica. The minimum usable concentration (0.03%) was defined as the lowest where specific binding of CTxB-labeled nanoparticles was still observed. (B) Gaussian-like (upper panel) and ring-like (lower panel) spatial distributions of confinement events at 0.03% GM1 on glass obtained by averaging 228 and 93 confinement events, respectively. For classification, each confinement site was fit to a Rayleigh distribution and the coefficient of determination, R^2 , was calculated. All confinement events with $R^2 > 0.95$ were included in the averaged Gaussian-like sites. As the sites with low R^2 values contain both ring-like confinement events and other non-Gaussian shapes, the ring-like sites were selected by thresholding the standard deviation of distances from the confinement center of mass over the overall confinement to be smaller than 0.45. The optimum ratio was determined visually by inspecting the resulting averaged spatial distributions. Horizontal cuts through the distributions are shown for clarity. Scale bar: 20 nm. (C) Individual ring-like confinement events exhibiting 3–5 distinct binding sites. The black lines represent trajectories after averaging 25 consecutive frames, equivalent to 0.5 ms time averaging, and help visualize the stepping motion between GM1 receptor sites. Scale bar: 20 nm. (D,E) Radial probability density plots and corresponding fits to a Rayleigh distribution for all confinement events recorded at 0.03% and 1.0% nt-GM1 concentrations. The distribution histograms were computed from 2×10^6 data points in each case. (F) Residuals from the fits of D and E as well as similar plots for 0.1 and 0.3% nt-GM1 concentration. (G) Change in the fwhm of Gaussian-like events as a function of nt-GM1 concentration. Error bars are the standard deviation of the mean confinement size.

ms, as inferred from $D = 1 \mu\text{m}^2/\text{s}$ of free diffusion, that is, an average travel of 200 nm in 10 ms. In contrast, all control experiments exhibited negligible confinement events and zero slope at $\Delta t > 100 \mu\text{s}$ in the corresponding log–log plots of diffusion coefficient versus time. The control experiments included the following: tracking biotinylated 1,2-dihexadecanoyl-*sn*-glycero-3-phosphoethanolamine (DPPE) in DOPC bilayers with streptavidin-functionalized AuNPs on plasma-cleaned glass substrates in the absence and presence of *nt*-GM1 (1.0% DPPE, 1.0% GM1); *DO*-GM1/CTxB at various receptor concentrations on plasma-cleaned glass (0.03 and 1% *DO*-GM1); and *nt*-GM1/CTxB on freshly cleaved mica (0.03% GM1) (Figure 4A). From this we follow that interleaflet coupling between GM1 in the lower and upper leaflets, combined with membrane–substrate interactions, is the reason for transient molecular confinement and thus anomalous diffusion. As mentioned, the hydroxyl-containing headgroups of GM1 lipids in the lower leaflet couple efficiently with hydroxyl groups on the plasma-cleaned surface. While DPPE has saturated chains that could potentially lead to interleaflet interactions, its headgroup does not contain hydroxyl groups for direct substrate interaction. *DO*-GM1 can interact with the substrate through its hydroxyl-containing headgroup, but its unsaturated tails do not exhibit strong interleaflet coupling. *nt*-GM1 has saturated tails and a hydroxyl-containing headgroup but cannot interact directly with the chemically inert mica surface. On the basis of the weak dependence of confinement on GM1 concentration, we conclude that although both substrate interactions and interleaflet coupling are required for anomalous diffusion, the number of confinement events is essentially independent of GM1 concentration and likely determined by the density of hydroxyl pinning sites on the surface. This conclusion is further supported by experiments showing that transient binding of *nt*-GM1-bound CTxB can be induced on mica by plasma cleaning the surface (Figure 4A, *pc-mica*), indeed suggesting that surface functionalization plays a critical role.

To examine the transient immobilization events in more detail we superimposed all confinement events for 0.03% GM1 on plasma-cleaned glass. We identified two different populations consisting of Gaussian-like and ring-like spatial distributions (Figure 4B) with confinement sizes < 20 nm. Individual ring-like confinement events often exhibited two to five distinct binding sites that were revisited frequently (Figure 4C) and showed little variation with label size (20 and 40 nm AuNP). To quantify any dependence on *nt*-GM1 concentration, we combined all confinement events and computed radial probability density plots as a function of *nt*-GM1 molar concentration ranging from 0.03 to 1.0% GM1. At 0.03% concentration (Figure 4D), the histogram obtained from a total of 2×10^6 data points was well described by a Rayleigh distribution, indicating that the confinement distributions were mostly Gaussian-like. As the GM1 concentration increased 33-fold to 1.0%, the fit to the Rayleigh distribution deteriorated (Figure 4E), a trend that scaled with *nt*-GM1 concentration (Figure 4F). In addition, for Gaussian-like events, although the number of confinement events did not change, the confinement size increased linearly with *nt*-GM1 concentration (Figure 4G).

Discussion. The unique ability of iSCAT to measure the motion of individual membrane components at their intrinsic time (μs) and length (nm) scales makes it an ideal method for investigating molecular membrane mobility. While other imaging approaches have contributed a great deal to our

understanding of the nanoscale structure and organization of cell membranes, potential experimental artifacts and poor spatiotemporal precision have impeded their ability to fully capture the behavior of membrane constituents. Because iSCAT induces minimal perturbations to the system being studied while providing high spatial and temporal resolution, it is able to capture nanoscopic behavior that is beyond the reach of other imaging approaches.

Given the possibility of defects in SLBs, it is important to emphasize that our results rule out bilayer imperfections as a cause for the observed behavior for a number of reasons. If defects were responsible, we would expect the same diffusive properties for *DO*-GM1 and *nt*-GM1 in contrast to experimental observations (Figures 2 and 3). Even in the event that differences in *DO*-GM1 and *nt*-GM1 lipid properties could cause a different propensity for the formation of defects at such low GM1 concentrations, such defects would also be present when tracking DPPE in an *nt*-GM1-doped SLB, an environment where we observed no anomalous diffusion (Figure 4A). DPPE-tracking in GM1-doped SLBs also shows that time-dependent mobilities induced by particle cross-linking or label-membrane interactions are unlikely. If the labels caused transient immobilization, anomalous subdiffusion would have been observed in the control experiments (Figure 4A). We also rule out nonspecific binding of the gold nanoparticle to the membrane, as particles not functionalized with CTxB did not interact with GM1-containing SLBs but were easily washed away. Comparison of the results obtained using inert and plasma-cleaned mica substrates excludes phase separation and nanoscopic aggregation due to free CTxB in solution as a possible cause for the transient immobilization. Our results therefore suggest that transient immobilization of GM1 in one leaflet can affect the diffusion of GM1-bound CTxB in the other leaflet through interactions between the lipid tails.

When we compare the mobility of *nt*-GM1 and *DO*-GM1 on cover glass with *nt*-GM1 on mica, we find that only the combination of *nt*-GM1 with a plasma-treated surface leads to time-dependent mobility. Our experiments on an effectively single component system also make effects due to lipid composition or substrate-induced asymmetry of the lipid distribution unlikely. A recent study of the distribution of GM1 in DOPC SLBs on UV/ozone-treated silica showed that 85% of the total GM1 is present in the upper leaflet with a linear relationship for 0–5% GM1 content.³⁸ Because the reported effect is a consequence of the lipid headgroup charge, *nt*-GM1 and *DO*-GM1 on glass would be expected to exhibit the same distribution between the two leaflets given that both experiments were performed on identical, plasma-cleaned glass substrates. Taken together, our results suggest that two conditions need to be met for anomalous diffusion: (a) GM1 molecules in the lower leaflet must be immobilized through interactions with the surface and (b) the immobilized molecules must interact with CTxB-cross-linked GM1 molecules in the upper leaflet through the hydrophobic core of the bilayer via long, straight aliphatic chains. How many cross-linked GM1 molecules are required for this to occur remains to be addressed in future work.

Our ability to super-resolve the spatiotemporal dynamics of the label during confinement events provides important clues to the nanoscopic origin of the observed anomalous diffusion. To illustrate this, it is helpful to consider the molecular details of the tracking assay. When drawn to scale, it is clear that for a nanoparticle label with a single CTxB subunit immobilized on

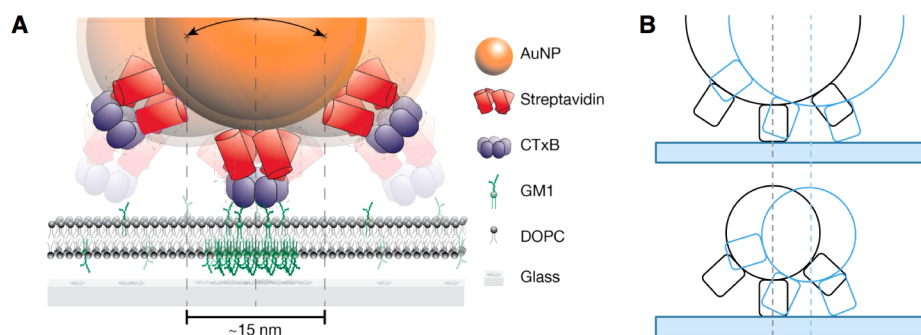


Figure 5. Transient binding of CTxB. (A) Schematic of the tracking assay during a transient binding event drawn to scale for a 20 nm AuNP. The curved arrow indicates the achievable nanoscopic rocking motion of the label and the dashed lines the achievable fluctuations in the center of mass of the label even for a completely immobilized CTxB. (B) Comparison of nanoscopic rocking motion for 20 and 40 nm labels. Due largely to the ratio between the radius of curvature of the particle and the separation between adjacent CTxB subunits, the confinement sizes are expected to be similar for both labels.

the membrane, some flexibility remains due to the distance between GM1 and the center of mass of the particle (Figure 5A). Simple geometric arguments suggest that nanoscopic rocking of the label can induce variations in the center of mass on the order of 15 nm for both 20 and 40 nm AuNPs (Figure 5B). When observed over tens of milliseconds, such fluctuations result in a 2D Gaussian spatial distribution around the center of mass if the position of the label can be determined on a time scale shorter than that of the rocking motion (Figure 4B). A second surface-bound CTxB on the nanoparticle may transiently bind to another, possibly diffusing GM1, and although the GM1/CTxB dissociation constant is very low ($K_d \approx 10^{-8}$), we frequently observed this behavior. On average, these multiple-bound particles yield trajectories centered around an immobilized central CTxB that resembles a ring-like structure on the nanoscale with a radius comparable to the maximum motion of the center of mass of the label (Figure 4C). This correspondence is illustrated by the cross sections shown in Figure 4B.

As multiple binding becomes more likely with increasing GM1 concentration, the radial probability density plot representative of all confinement events is expected to further deviate from a Rayleigh distribution. At low GM1 concentration (0.03%), there is ~ 1 receptor in an area of 40 nm^2 , meaning that other CTxB subunits on the AuNP will rarely encounter any GM1 receptors upon approaching the membrane during nanoscopic rocking. As a result, we obtain an excellent fit to a Rayleigh distribution ($R^2 > 0.95$) (Figure 4D,E). Upon increasing the receptor concentration 30-fold, however, the immediate presence of GM1 becomes more likely and transient binding to individual receptors occurs more often. As a consequence, the deviation between the radial probability density histogram and the Rayleigh fit increases with GM1 concentration. Even for Gaussian-like confinement events, an increase in nearby GM1 concentration should lead to an increase in the apparent confined area because nanoscopic rocking will result in the particle on average spending more time near the membrane surface due to transient binding with additional GM1 (Figure 4G), even if it does not lead to cross-linking and long-term multiple binding.

The tight lateral confinement on the $<20 \text{ nm}$ scale and the observation of ring-like confinement events are both consistent with transient immobilization of a single membrane-bound CTxB subunit on the nanometer scale. Given that transient binding requires both native GM1 lipid tail domains and a

plasma-cleaned substrate as evidenced by the studies on mica and with DO-GM1, we propose that the most likely origin is clustering of GM1 on the lower leaflet by hydrogen bonding to nanoscopic patches of surface hydroxyl groups from the plasma cleaning process. Although in principle one could envision that a single pinned GM1 molecule is responsible for immobilization of five CTxB-bound GM1 molecules in the upper leaflet, such a prospect appears energetically unlikely. We conclude that the lower leaflet is likely scattered with numerous $<10 \text{ nm}$ patches of high GM1 density with higher viscosity that communicate with the upper leaflet through transbilayer interactions, leading to transient ($<10 \text{ ms}$) nanoscopic confinement.

This interpretation is further supported by the weak dependence of the observed confinement events on label size. Both 20 and 40 nm labels produce similarly sized confinement events in line with expectations based on the schematic in Figure 5B, a consequence largely of the ratio between the radius of curvature and the separation between adjacent CTxB subunits. The proposal of nanoscopic aggregates of GM1 on plasma-cleaned glass also agrees with AFM measurements of comparable assays, although these do not provide direct information regarding whether the aggregation occurs in the lower or upper leaflet of the bilayer.²⁷ Our general mechanism agrees with early observations of interleaflet coupling,³⁹ although these required the presence of macroscopic domains. Taken together, our work suggests that transient binding can occur for nanoscopic domains and change the mobility of single proteins bound to multiple receptors across a bilayer membrane.

Materials and Methods. Materials. The compounds 1,2-dioleoyl-*sn*-glycero-3-phosphocholine (DOPC), 1,2-dihexadecanoyl-*sn*-glycero-3-phosphoethanolamine-*N*-(cap biotinyl) (DPPE), and GM1 bovine brain ganglioside (GM1) were purchased from Avanti Polar Lipids (Alabaster, AL). DO-GM1 was prepared as described before.⁹ Biotin-labeled cholera toxin B (CTxB) subunits from *Vibrio cholera* were purchased from Sigma-Aldrich (Milwaukee, WI) and reconstituted with water to give a solution containing 0.05 M Tris buffer, pH 7.5, 0.2 M NaCl, 3 mM NaN_3 , and 1 mM sodium EDTA. Gold nanoparticles (AuNPs) functionalized with streptavidin were purchased from British Biocell International (Cardiff, U.K.), diluted to a concentration of 9×10^{10} particles/ml and incubated with a 10-fold excess of biotin-CTxB at room temperature for 1 h. Excess CTxB was removed by centrifuging

the AuNP/CTxB sample for 2 min at 14000g and resuspending the pellet in bilayer buffer (10 mM HEPES, pH 6.8, 200 mM NaCl and 2 mM CaCl₂). On the basis of a streptavidin contact area of 25 nm², and assuming that streptavidin covers 50% of the surface area of an AuNP, we estimate that there are 25 CTxB per 20 nm AuNP and 100 CTxB per 40 nm AuNP. For DPPE tracking experiments, streptavidin-functionalized AuNPs were added directly to the bilayer.

Vesicle Preparation. Small unilamellar vesicles (SUVs) were prepared by the vesicle extrusion method. Lipids in organic solvent were mixed in a glass vial and the solvent evaporated first under a gentle stream of nitrogen for 5 min and then under vacuum for 30 min. The dried lipid film was resuspended to a lipid concentration of 1 mg/mL in bilayer buffer. Lipid suspensions were vortexed for 1 min, hydrated at room temperature for 30 min and then passed 21 times through a 100 nm polycarbonate membrane using a mini extruder (Avanti Polar Lipids), resulting in clear suspensions of SUVs. SUVs were stored at 4 °C and used within 24 h.

Substrate Preparation. No. 1.5 borosilicate cover glass (Menzel-Gläser, Braunschweig, Germany) was etched in 2:1 H₂O₂:HCl for 10 min, followed by thorough rinsing with ultrapure water (Merck Millipore, Billerica, MA). The clean substrates were dried with a gentle stream of nitrogen and etched with oxygen plasma for 8 min at 50 W power immediately prior to vesicle deposition (Diener Electronic, Plasma System Femto). Mica substrates were prepared by bonding a 22 mm square sheet of mica (Agar Scientific, Essex, U.K.) to a clean cover glass using optical adhesive (Norland Optical Adhesive 61). Immediately prior to vesicle deposition, the mica was cleaved leaving a thin, optically transparent layer adhered to the cover glass.

Supported Lipid Bilayer Formation. Sample chambers were assembled by placing a CultureWell silicon gasket (Grace Bio-Laboratories, Bend, OR) onto the glass or mica substrate. SLBs were formed by adding 20 μL bilayer buffer followed by 10 μL of the 1 mg/mL SUV suspension to the 30 μL sample well and incubating for 5 min. Excess SUVs were rinsed away with 3 mL bilayer buffer and then 2.5 μL of AuNP/CTxB or AuNP/streptavidin solution was deposited and allowed to incubate for 5 min. Excess particles were rinsed away with 1 mL bilayer buffer prior to imaging.

Instrument Setup. A collimated beam from a solid-state diode laser ($\lambda = 532$ nm) was focused through an under-filled 60×, 1.42 NA oil immersion microscope objective (Olympus) onto a small region of the sample. A portion of the light scattered from the AuNP together with the incident light reflected at the membrane/water interface was collected by the objective and focused onto a fast CMOS camera (Photon Focus MV-D1024-160-CL-8, Lachen, Switzerland) for imaging with 100× magnification for an effective pixel size of 106 nm. The incident power density was between 20 and 30 kW/cm², which corresponds to focusing approximately 3 mW onto a 2 × 2 μm² spot size at the sample. For a 20 nm AuNP, this incident intensity at a wavelength of 532 nm leads to a local heating effect that amounts to a <1.5 K rise in temperature at the particle surface.²² We remark that any trapping forces exerted by this beam are on the order of few femtonewtons,⁴⁰ much too small to affect the diffusion on the length scales studied in this work.

Mean-Squared Displacement Analysis. For all trajectories, the two-dimensional MSD for each time interval was calculated according to

$$\text{MSD}(\Delta t_n) = \frac{1}{N - n - 1} \sum_{j=1}^{N-n-1} [\vec{r}(\Delta t_{j+n}) - \vec{r}(\Delta t_j)]^2$$

where $\Delta t = 20 \mu\text{s}$ (frame time), $|\vec{r}(\Delta t_{j+n}) - \vec{r}(\Delta t_j)|$ is the particle displacement during time interval $\Delta t_n = n\Delta t$, N is the total number of frames in the trajectory, and n is a positive integer that determines the time interval. The log-log plots of the diffusion coefficient versus time (Figures 2, 3) were generated using intervals up to 20% of the trajectory length.

Nanoscope Localization and Tracking. Particle detection was performed by combining the nonmaximum suppression algorithm with a threshold based on the median absolute deviation. Briefly, the standard deviation of the image in the absence of particles was estimated by the median absolute deviation. Pixel values exceeding three times this standard deviation were classified as candidate pixels for particles. The candidate pixels from the median absolute deviation threshold were intersected with the candidate pixels from the non-maximum suppression algorithm to obtain to the nearest integer pixel value the position of any candidate particle. Candidate particles were then segmented into regions of interest corresponding to 954 × 954 nm², which for a magnification of 100× corresponded to 9 × 9 pixels (effective pixel size of 106 nm). A two-dimensional Gaussian function was then fit to each segmented region and candidate particles satisfying the contrast upper and lower bounds were used as input parameters for the consecutive frame. Particle trajectories were reconstructed using a greedy algorithm that minimized the distance between detected particle positions in consecutive frames. Given the density of less than one AuNP/CTxB complex per square micrometer, any artifacts arising due to this greedy algorithm were minimized.

AUTHOR INFORMATION

Corresponding Author

*E-mail: philipp.kukura@chem.ox.ac.uk. Phone: +44 18652-75401.

Present Address

(K.M.S.) Division of Immune Cell Biology, MRC National Institute for Medical Research, The Ridgeway, Mill Hill, London NW7 1AA, U.K.

Author Contributions

^{||}K.M.S. and J.O.-A. contributed equally to this work.

Notes

The authors declare no competing financial interest.

ACKNOWLEDGMENTS

P.K. is supported by the John Fell Fund, a career acceleration fellowship from the EPSRC (EP/H003531) and an ERC starting grant (NanoScope). K.M.S. was supported by a fellowship from the National Institute of Biomedical Imaging and Bioengineering, National Institutes of Health (FEB013960). J.O.A. was supported by a scholarship from CONACyT to pursue his doctoral work (scholar: 213546).

REFERENCES

- (1) Dustin, M. L.; Groves, J. T. *Annu. Rev. Biophys.* **2012**, *41*, 543–556.
- (2) Sourjik, V. *Trends Microbiol.* **2004**, *12*, 569–576.
- (3) Ewers, H.; Helenius, A. *Cold Spring Harbor Perspect. Biol.* **2011**, *3*, a004721.
- (4) Liu, A. P.; Fletcher, D. A. *Biophys. J.* **2006**, *91*, 4064–4070.

- (5) Klotzsch, E.; Schütz, G. J. *Philos. Trans. R. Soc. London, Ser. B* **2012**, 368, 20120033.
- (6) Baumgart, T.; Hess, S. T.; Webb, W. W. *Nature* **2003**, 425, 821–824.
- (7) Römer, W.; Berland, L.; Chambon, V.; Gaus, K.; Windschiegel, B.; Tenza, D.; Aly, M. R.; Fraissier, V.; Florent, J. C.; Perrais, D.; Lamaze, C.; Raposo, G.; Steinem, C.; Sens, P.; Bassereau, P.; Johannes, L. *Nature* **2007**, 450, 670–675.
- (8) Liu, J.; Sun, Y.; Drubin, D. G.; Oster, G. F. *PLoS Biol.* **2009**, 7, e1000204.
- (9) Ewers, H.; Römer, W.; Smith, A. E.; Bacia, K.; Dmitrieff, S.; Chai, W.; Mancini, R.; Kartenbeck, J.; Chambon, V.; Berland, L.; Oppenheim, A.; Schwarzmam, G.; Feizi, T.; Schwille, P.; Sens, P.; Helenius, A.; Johannes, L. *Nat. Cell Biol.* **2010**, 12, 11–18.
- (10) Wan, C.; Kiessling, V.; Tamm, L. K. *Biochemistry* **2008**, 47, 2190–2198.
- (11) Collins, M. D.; Keller, S. L. *Proc. Natl. Acad. Sci. U.S.A.* **2008**, 105, 124–128.
- (12) Honigsmann, A.; Sadeghi, S.; Keller, J.; Hell, S. W.; Eggeling, C.; Vink, R. *eLife* **2014**, 3, e01671.
- (13) Eggeling, C.; Ringemann, C.; Medda, R.; Schwarzmam, G.; Sandhoff, K.; Polyakova, S.; Belov, V. N.; Hein, B.; von Middendorff, C.; Schönle, A.; Hell, S. W. *Nature* **2009**, 457, 1159–1162.
- (14) Wawrezynieck, L.; Rigneault, H.; Marguet, D.; Lenne, P. F. *Biophys. J.* **2005**, 89, 4029–4042.
- (15) Fujiwara, T.; Ritchie, K.; Murakoshi, H.; Jacobson, K.; Kusumi, A. *J. Cell Biol.* **2002**, 157, 1071–1081.
- (16) Murase, K.; Fujiwara, T.; Umemura, Y.; Suzuki, K.; Iino, R.; Yamashita, H.; Saito, M.; Murakoshi, H.; Ritchie, K.; Kusumi, A. *Biophys. J.* **2004**, 86, 4075–4093.
- (17) Mascalchi, P.; Haanappel, E.; Carayon, K.; Mazères, S.; Salomé, L. *Soft Matter* **2012**, 8, 4462–4470.
- (18) Martin, D. S.; Forstner, M. B.; Käs, J. A. *Biophys. J.* **2002**, 83, 2109–2117.
- (19) Wieser, S.; Moertelmaier, M.; Fuertbauer, E.; Stockinger, H.; Schütz, G. J. *Biophys. J.* **2007**, 92, 3719–3728.
- (20) Adler, J.; Shevchuk, A. L.; Novak, P.; Korchev, Y. E.; Parmryd, I. *Nat. Methods* **2010**, 7, 170–171.
- (21) Kukura, P.; Ewers, H.; Müller, C.; Renn, A.; Helenius, A.; Sandoghdar, V. *Nat. Methods* **2009**, 6, 923–927.
- (22) Ortega-Arroyo, J.; Kukura, P. *Phys. Chem. Chem. Phys.* **2012**, 14, 15625–15636.
- (23) Sackmann, E. *Science* **1996**, 271, 43–48.
- (24) Crespo, P. M.; von Muhlinen, N.; Iglesias-Bartolomé, R.; Daniotti, J. L. *FEBS J.* **2008**, 275, 6043–6056.
- (25) Chinnapen, D. J. F.; Hsieh, W. T.; te Welscher, Y. M.; Saslowsky, D. E.; Kaoutzani, L.; Brandsma, E.; D'Auria, L.; Park, H.; Wagner, J. S.; Drake, K. R.; Kang, M.; Benjamin, T.; Ullman, M. D.; Costello, C. E.; Kenworthy, A. K.; Baumgart, T.; Massol, R. H.; Lencer, W. I. *Dev. Cell* **2012**, 23, 573–586.
- (26) Gupta, N.; DeFranco, A. L. *Mol. Biol. Cell* **2003**, 14, 432–444.
- (27) Shi, J.; Yang, T.; Kataoka, S.; Zhang, Y.; Diaz, A. J.; Cremer, P. S. *J. Am. Chem. Soc.* **2007**, 129, 5954–5961.
- (28) Lingwood, D.; Ries, J.; Schwille, P.; Simons, K. *Proc. Natl. Acad. Sci. U.S.A.* **2008**, 105, 10005–10010.
- (29) Dietrich, C.; Volovyk, Z. N.; Levi, M.; Thompson, N. L.; Jacobson, K. *Proc. Natl. Acad. Sci. U.S.A.* **2001**, 98, 10642–10647.
- (30) Mueller, V.; Ringemann, C.; Honigsmann, A.; Schwarzmam, G.; Medda, R.; Leutenegger, M.; Polyakova, S.; Belov, V. N.; Hell, S. W.; Eggeling, C. *Biophys. J.* **2011**, 101, 1651–1660.
- (31) Hsieh, C. L.; Spindler, S.; Ehrig, J.; Sandoghdar, V. *J. Phys. Chem. B* **2014**, 118, 1545–1554.
- (32) Lindfors, K.; Kalkbrenner, T.; Stoller, P.; Sandoghdar, V. *Phys. Rev. Lett.* **2004**, 93, 037401.
- (33) Thompson, R. E.; Larson, D. R.; Webb, W. W. *Biophys. J.* **2002**, 82, 2775–2783.
- (34) Considine, P. S. *J. Opt. Soc. Am.* **1966**, 56, 1001–1007.
- (35) Saxton, M. J.; Jacobson, K. *Annu. Rev. Biophys. Biomol. Struct.* **1997**, 26, 373–399.
- (36) DeRosa, R. L.; Schader, P. A.; Shelby, J. E. *J. Non-Cryst. Solids* **2003**, 331, 32–40.
- (37) Savin, T.; Doyle, P. S. *Biophys. J.* **2005**, 88, 623–638.
- (38) Carton, I.; Malinina, L.; Richter, R. P. *Biophys. J.* **2010**, 99, 2947–2956.
- (39) Seul, M.; Subramaniam, S.; McConnell, H. M. *J. Phys. Chem.* **1985**, 89, 3592–3595.
- (40) Fedoruk, M.; Lutich, A. A.; Feldmann, J. *ACS Nano* **2011**, 5, 7377–7382.
- (41) Lin, Y. H.; Chang, W. L.; Hsieh, C. H. *Opt. Express* **2014**, 22, 9159–9170.

■ NOTE ADDED IN PROOF

Tracking of 20 nm gold particles with iSCAT on bilayer membranes was recently demonstrated with 2 nm spatial precision at 500 kHz frame rates.⁴¹